2D Nano-Sonosensitizers Facilitate Energy Transfer to Enhance Sonodynamic Therapy

*Gan Lin, Geoffrey T. Nash, Taokun Luo, Indranil Ghosh, Siddhartha Sohoni, Andrew J. Christofferson, Gang Liu, Gregory S. Engel, and Wenbin Lin**

Although sonodynamic therapy (SDT) has shown promise for cancer treatment, the lack of efficient sonosensitizers (SSs) has limited the clinical application of SDT. Here, a new strategy is reported for designing efficient nano-sonosensitizers based on 2D nanoscale metal–organic layers (MOLs). Composed of Hf-oxo secondary building units (SBUs) and iridium-based linkers, the MOL is anchored with 5,10,15,20-tetra(p-benzoato) porphyrin (TBP) sensitizers on the SBUs to afford TBP@MOL. TBP@MOL shows 14.1- and 7.4-fold higher singlet oxygen ($^1O_2$) generation than free TBP ligands and Hf-TBP, a 3D nanoscale metal–organic framework, respectively. The $^1O_2$ generation of TBP@MOL is enhanced by isolating TBP SSs on the SBUs of the MOL, which prevents aggregation-induced quenching of the excited sensitizers, and by triplet–triplet Dexter energy transfer between excited iridium-based linkers and TBP SSs, which more efficiently harnesses broad-spectrum sonoluminescence. Anchoring TBP on the MOL surface also enhances the energy transfer between the excited sensitizer and ground-state triplet oxygen to increase $^1O_2$ generation efficacy. In mouse models of colorectal and breast cancer, TBP@MOL demonstrates significantly higher SDT efficacy than Hf-TBP and TBP. This work uncovers a new strategy to design effective nano-sonosensitizers by facilitating energy transfer to efficiently capture broad-spectrum sonoluminescence and enhance $^1O_2$ generation.

1. Introduction

Sonodynamic therapy (SDT) utilizes ultrasonic cavitation to produce broad-spectrum sonoluminescence that can excite sonosensitizers (SSs) for the generation of cytotoxic reactive oxygen species (ROS).[1–4] With significantly increased tissue penetration depth, SDT has emerged as a promising alternative modality to photodynamic therapy (PDT).[5–12] Although organic sensitizers such as porphyrins are efficacious for PDT, they have proven inadequate for SDT, likely due to their nonideal tumor uptake, low solubility in physiological environments, and, more importantly, the very low emission intensity of sonoluminescence compared to direct light irradiation in PDT.[13–17] Low aqueous solubility of SSs leads to aggregation-induced quenching (AIQ) of their excited states, which impairs ROS generation.[18,19] Nanotechnology has been used to isolate and deliver SSs to reduce AIQ and increase bioavailability.[20–25]

Nanoscale metal–organic frameworks (MOFs) have provided an exceptionally versatile platform for designing nano-photosensitizers for PDT owing to their structural tunability, porosity, and ability to isolate organic photosensitizers in high loadings in a rigid framework.[26–34] However, MOFs have not been extensively explored as nano-sonosensitizers for SDT and have shown only modest SDT efficacy to date.[35–39] Unlike MOF-based nano-photosensitizers, no established methods exist to

G. Lin, G. T. Nash, T. Luo, I. Ghosh, S. Sohoni, G. S. Engel, W. Lin
Department of Chemistry
The University of Chicago
Chicago, IL 60637, USA
E-mail: wenbinlin@uchicago.edu

G. Lin, G. Liu
State Key Laboratory of Molecular Vaccinology and Molecular
Diagnostics & Center for Molecular Imaging and Translational Medicine
School of Public Health
Xiamen University
Xiamen 361102, China

The ORCID identification number(s) for the author(s) of this article can be found under https://doi.org/10.1002/adma.202212069.

A. J. Christofferson
School of Science
College of Science, Engineering and Health
RMIT University
Melbourne, Victoria 3001, Australia

G. S. Engel
Pritzker School of Molecular Engineering
The University of Chicago
Chicago, IL 60637, USA

W. Lin
Department of Radiation and Cellular Oncology
and Ludwig Center for Metastasis Research
The University of Chicago
Chicago, IL 60637, USA

ADVANCED
SCIENCE NEWS
www.advancedsciencenews.com

ADVANCED
MATERIALS
www.advmat.de

improve and optimize ROS generation from SS-loaded MOFs under ultrasound (US) irradiation.

Here we report the design of a new 2D nanoscale metal–organic layer (MOL), TBP@MOL, for enhanced singlet oxygen ($^1O_2$) generation. TBP@MOL was prepared by anchoring 5,10,15,20-tetra(p-benzoato)porphyrin (TBP) sensitizers to the Hf_{12} secondary building units (SBUs) of the MOL comprising Hf_{12} SBUs and Ir(DBB)[dF(CF$_3$)ppy]$^{2+}$ bridging ligands (DBB-Ir, DBB: 4,4′-di(4-benzoato)-2,2′-bipyridine; dF(CF$_3$)ppy: 2-(2,4-difluorophenyl)-5-(trifluoromethyl)-pyridine). Under US irradiation, TBP@MOL shows 14.1- and 7.4-fold higher $^1O_2$ generation than TBP and Hf-TBP, a 3D TBP-based MOF, respectively. With proximity of TBP sensitizers to the DBB-Ir donor ligands (≈10 Å) via flexible TBP attachment to the SBUs, TBP@MOL enables effective SDT via triplet–triplet Dexter energy transfer from excited DBB-Ir to SBU-anchored TBP sensitizers and enhances energy transfer between excited triplet-state TBP and ground-state triplet oxygen ($^3O_2$). Consequently, TBP@MOL displays significantly higher SDT efficacy than its Hf-TBP and free TBP counterparts on mouse models of colon and breast cancer.

2. Results and Discussion

TBP@MOL was synthesized in two steps (**Figure 1**). Free-standing Hf_{12}-DBB-Ir MOL was synthesized as previously reported through a solvothermal reaction between HfCl$_4$ and DBB-Ir in N,N-dimethylformamide (DMF) at 80 °C with trifluoroacetic acid (TFA) and water as modulators (Figures S1–S6, Supporting Information).[40] The MOL is built from an infinite 2D network of Hf_{12} SBUs laterally bridged by DBB-Ir and vertically terminated by TFA capping agents to afford a monolayer structure with **kgd** topology and the formula $Hf_{12}(\mu_3\text{-}O)_8(\mu_3\text{-}OH)_8(\mu_2\text{-}OH)_6(DBB\text{-}Ir\text{-}F)_6(TFA)_6$. ^{19}F NMR analysis of the digested MOL confirmed the DBB-Ir to TFA ratio of 1:1 (Figures S5 and S6, Supporting Information). Transmission electron microscopy (TEM) and atomic force microscopy (AFM) imaging of the MOL confirmed the monolayer morphology with a diameter of ≈250 nm and a thickness of ≈1.8 nm (Figure S4, Supporting Information).

TBP SSs were covalently anchored to the MOL by partially replacing TFA capping agents on Hf_{12} SBUs via carboxylate exchange to afford TBP@MOL with the formula $(TBP)_{1.7}@$ $Hf_{12}(\mu_3\text{-}O)_8(\mu_3\text{-}OH)_8(\mu_2\text{-}OH)_6(DBB\text{-}Ir\text{-}F)_6(TFA)_{4.3}$ (**Figure 2**; Figure S7, Supporting Information). ^{19}F NMR analysis of digested TBP@MOL displayed a decreased TFA to DBB-Ir ratio compared to the MOL, supporting the partial replacement of TFA with TBP on the MOL (Figures S7–S10, Supporting Information). The remaining TFA signal in the ^{19}F NMR spectrum indicates that the large size of TBP prevented complete replacement of all TFA groups (Figure S10, Supporting Information). Upon TBP conjugation to the cationic MOL, the zeta (ζ) potential reversed from +38.5 ± 1.0 to
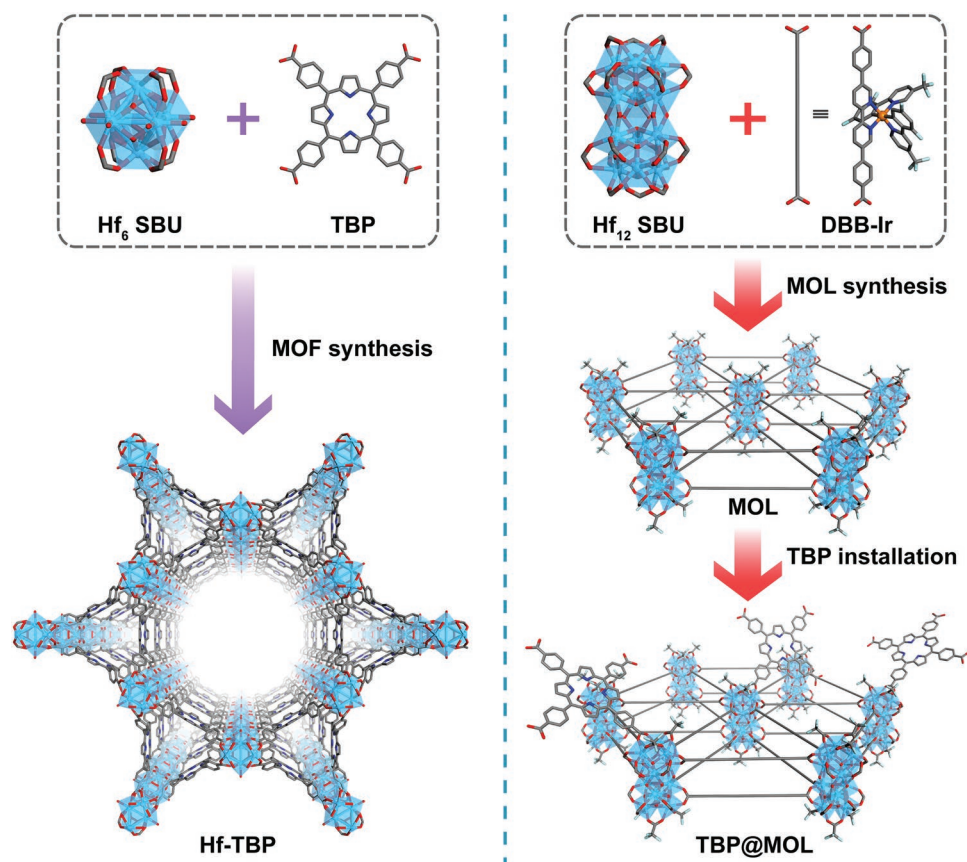

Figure 1. Synthetic scheme of Hf-TBP (left) and TBP@MOL (right). TBP SSs are rigidly confined in the 3D framework of Hf-TBP but flexibly anchored to the SBUs of the 2D MOL in TBP@MOL (orange: Ir, sky blue: Hf, pale light blue: F, red: O, blue: N, gray: C; H atoms are omitted for clarity).
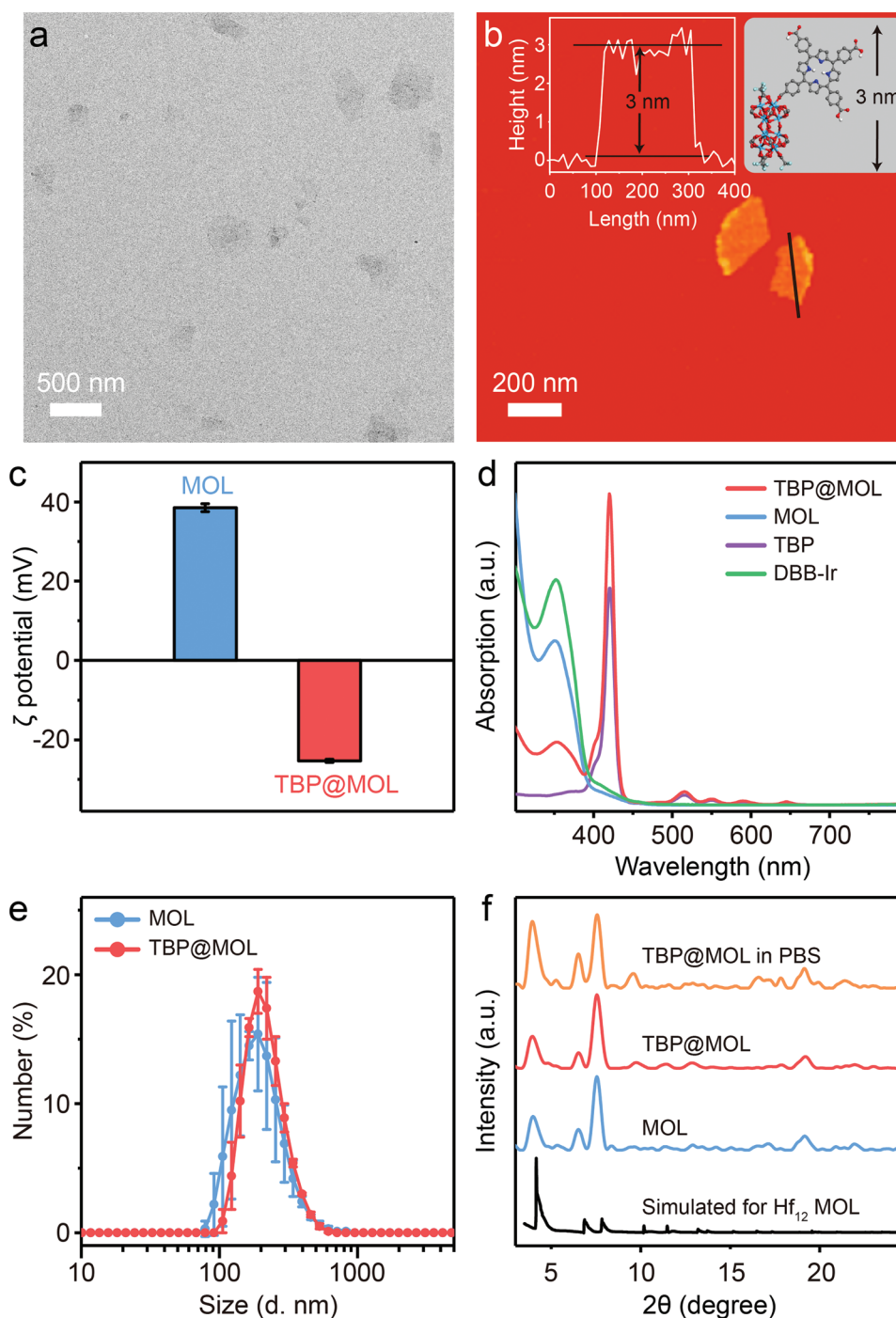
Figure 2. a) TEM image of TBP@MOL. b) AFM topographic image, height profile (inset, left), and modeled height (inset, right) of TBP@MOL. c) Zeta (ζ) potentials of MOL and TBP@MOL in water. d) Normalized UV–vis absorption spectra of TBP, DBB-Ir, MOL, and TBP@MOL in dimethyl sulfoxide (DMSO). e) Number-averaged diameters of MOL and TBP@MOL in ethanol. f) PXRD patterns of MOL, as-synthesized TBP@MOL, and TBP@MOL after soaking in phosphate-buffered saline (PBS) for 24 h and the simulated pattern of Hf_{12}-MOL.

−25.3 ± 0.4 mV, consistent with the surface loading of anionic TBP (Figure 2c). The presence of both TBP and DBB-Ir in TBP@MOL was supported by their characteristic UV–vis absorption peaks and their ^1H NMR signals in the digested TBP@MOL (Figure 2d; Figure S8, Supporting Information). Dynamic light scattering (DLS) measurements gave

number-averaged sizes of 221.0 ± 5.7 and 203.7 ± 21.0 for the MOL and TBP@MOL, respectively (Figure 2e).

The powder X-ray diffraction (PXRD) pattern of TBP@MOL matched well with that of the MOL and the simulated pattern for the Hf_{12} MOL structure model (Figure 2f). TEM imaging indicated that TBP@MOL retained the monolayer morphology

2212069 (3 of 9)

of the MOL, with a diameter of ≈250 nm (Figure 2a). AFM imaging of TBP@MOL displayed a thickness of ≈3.0 nm, which is consistent with the modeled height of a Hf_{12} SBU capped with a TBP ligand (Figure 2b). TBP@MOL was stable and retained its crystallinity after US irradiation in water (3.4 MHz, 1.0 or 2.0 W cm^{-2}, 50% duty cycle, and 10 min; Figure S13, Supporting Information). The TBP loading was calculated to be 12.3 wt% based on UV–vis absorption spectroscopy (Figure S11, Supporting Information) and inductively coupled plasma-mass spectrometry (ICP-MS), corresponding to a TBP: Hf_{12} SBU ratio of 1.7:1.

A TBP-based MOF, Hf-TBP, with TBP SSs rigidly confined between SBUs within the 3D framework, was synthesized as previously reported.[41] Hf-TBP has a **csq** topology and the formula $Hf_6(\mu_3\text{-O})_4(\mu_3\text{-OH})_4(OH)_4(H_2O)_4(\mu_2\text{-TBP})_2$ (Figure S20, Supporting Information). Hf-TBP exhibited a rod-like morphology by TEM and displayed a number-averaged size of 108.7 ± 7.4 nm by DLS (Figure S21, Supporting Information).

The $^1O_2$ generation efficiency of the different TBP systems was determined by singlet oxygen sensor green (SOSG) assay. Under US irradiation (3.4 MHz, 1.0 W cm^{-2}, 50% duty cycle, and 10 min) in water, TBP@MOL generated 14.1- and 7.4-fold higher $^1O_2$ than TBP and Hf-TBP, respectively (**Figure 3**a). Because sonoluminescence is a broad-spectrum emission (≈300–700 nm), the MOL itself showed some $^1O_2$ generation due to direct excitation of DBB-Ir linkers (Figures S39 and S40, Supporting Information). However, a physical mixture of TBP and the MOL generated 3.1-fold lower $^1O_2$ than TBP@MOL. Under US irradiation, TBP@MOL also showed eightfold higher SOSG signal than a commonly studied water-soluble SS, rose bengal, demonstrating its superior $^1O_2$ generation over traditional organic SSs. A similar trend was observed for the MOL modified with a related porphyrin sensitizer, 5,15-di(p-benzoato) porphyrin (DBP) (Figures S14–S19 and S22–S24, Supporting Information). DBP@MOL showed 15.0- and 4.8-fold higher $^1O_2$ generation than DBP and 3D Hf-DBP MOF,[42] respectively, under US irradiation (Figure S38, Supporting Information).

The enhanced $^1O_2$ generation of TBP@MOL was confirmed by in vitro SDT studies. US irradiation (3.4 MHz, 1 W cm^{-2}, 50% duty cycle, and 5 min; "+" and "−" denote with and without US irradiation, respectively) caused negligible cytotoxicity to CT26 colorectal and 4T1 triple-negative breast cancer cells (Figure S45, Supporting Information). TBP@MOL with US irradiation (denoted TBP@MOL(+)) induced significant cytotoxicity with half maximal inhibitory concentration (IC_{50}) values of 6.0 and 6.1 μM for CT26 and 4T1 cells, respectively (Figure 3c,d; Tables S1 and S2, Supporting Information). These (IC_{50}) values were 5.6- and 5.5-fold lower than those of TBP(+), respectively, and 12.3- and 5.6-fold lower than those of Hf-TBP(+), respectively. Without US irradiation, TBP, MOL, and TBP@MOL showed minimal toxicity at concentrations of up to 40 μM (Figure S46, Supporting Information), indicating low intrinsic toxicity of TBP@MOL. The MOL itself displayed low cytotoxicity with and without US irradiation (Figure S47, Supporting Information), further supporting that the enhanced toxicity of TBP@MOL largely stems from efficient $^1O_2$ generation of SBU-anchored TBP.[43]

The enhanced SDT efficacy of TBP@MOL was supported by calcein–acetoxymethyl (AM)/propidium iodide (PI) staining under confocal laser scanning microscope (CLSM) imaging. TBP@MOL(+)-treated CT26 cells showed much stronger signals of PI, but weaker fluorescence of calcein-AM than other groups (Figure 3e; Figure S48, Supporting Information), indicating significantly enhanced cancer cell killing by TBP@MOL(+). US-stimulated generation of ROS was evaluated by dichloro-fluorescein diacetate (DCFDA) in CT26 cells. After US irradiation, obvious green fluorescence of DCF was observed in TBP@MOL(+)-treated CT26 cells while other treatment groups showed little DCF fluorescence (Figure 3f; Figure S49, Supporting Information). Flow cytometry analysis showed that TBP@MOL(+) generated more than an order of magnitude higher ROS than the other systems (Figure S50, Supporting Information), likely due to increased cellular uptake of and enhanced $^1O_2$ generation by TBP@MOL (Figure S51, Supporting Information). The slightly higher intracellular uptake of TBP@MOL compared to Hf-TBP was likely due to the smaller dimension of TBP@MOL.[44]

SDT-induced apoptosis was evaluated with the Annexin V/PI kit by flow cytometry. At an equivalent TBP concentration of 10 μM, TBP@MOL(+)-treated cells showed more severe apoptotic cell death with only 64.7% healthy cells remaining compared to 98.0% and 97.4% in cells treated with Hf-TBP(+) and TBP(+), respectively (Figure 3g). More than 98% of healthy cells were present in the treatment groups without US irradiation. US irradiation alone did not cause cell death (Figure S52, Supporting Information). Taken together, TBP@MOL is a significantly more efficient SS than free TBP and Hf-TBP.

Since US excitation of the SSs proceeds mainly via sonoluminescence, we compared the photoexcitation dynamics of the various SS systems to understand how the SBU-anchored TBP in TBP@MOL enhances $^1O_2$ generation over the other TBP systems. Steady-state emission spectra (λ_{ex} = 420 nm) showed a significant reduction of TBP emission intensity in Hf-TBP and TBP@MOL (**Figure 4**b). This result is supported by the time-correlated single photon counting (TCSPC) decay profiles, which yielded shorter average fluorescence lifetimes (τ_{avg}) of 3.12 and 3.33 ns for TBP@MOL and Hf-TBP, respectively, compared to a τ_{avg} of 9.52 ns for TBP (Figure 4c; Tables S3 and S4, Supporting Information). To investigate the origins of the 1–2 ns time constants for TBP@MOL and Hf-TBP, we conducted broadband transient absorption (TA) experiments. We see a strong and broad excited state absorption feature, which we attribute to the S_1 state.[33,34] The ≈2 ns time constant extracted from the TA experiments originates from the decay of the excited state absorption feature for both Hf-TBP and TBP@MOL (Figure 4e,f; Table S6, Supporting Information). We associate this short time constant with nonradiative decay via coupling between TBP and Hf, which facilitates intersystem crossing (ISC)[45,46] from the excited singlet state (S_1) to the triplet state (T_1). This time constant is absent in the free TBP and could therefore be attributed to orientational quenching of the excited singlet state via the phonon modes in the crystalline frameworks.[47] While the inefficient $^1O_2$ generation of TBP can be explained by AIQ in aqueous environments, similarly facile ISC between TBP@MOL and Hf-TBP fails to explain their vastly different $^1O_2$ generation efficiency.

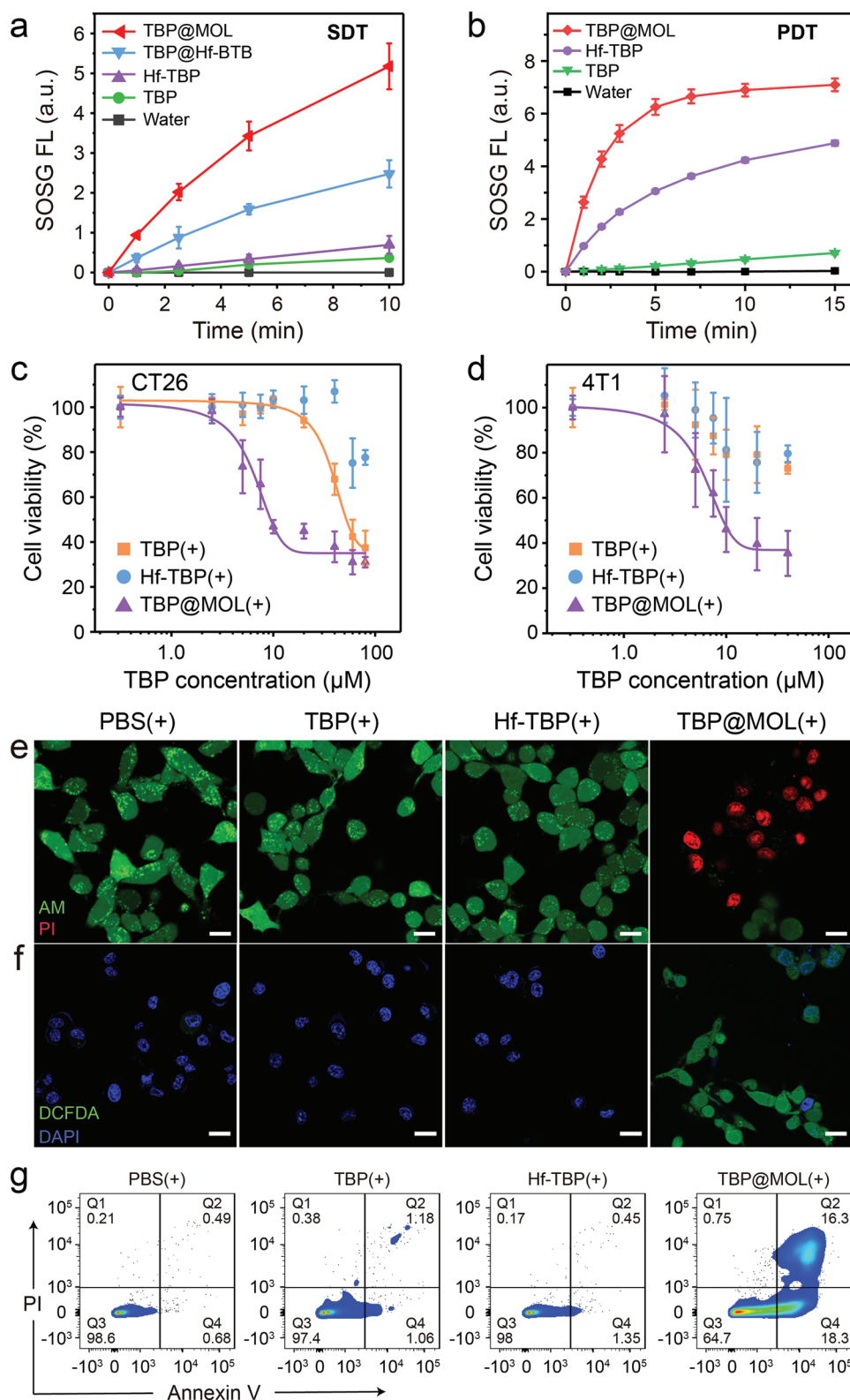To eliminate the contribution of DBB-Ir linkers in SDT of TBP@MOL, we determined $^1O_2$ generation of different TBP

Figure 3. $^1O_2$ generation of different TBP systems upon a) US and b) light irradiation as detected by SOSG assay. Cell viability assays of TBP(+), Hf-TBP(+), and TBP@MOL(+) in c) CT26 and d) 4T1 cells upon US irradiation ($n = 4$). CLSM images showing e) calcein-AM/PI staining and f) DCFDA staining and flow cytometric analyses showing g) Annexin V/PI staining in CT26 cells after PBS(+), TBP(+), Hf-TBP(+), or TBP@MOL(+) treatment. Scale bar = 20 µm.
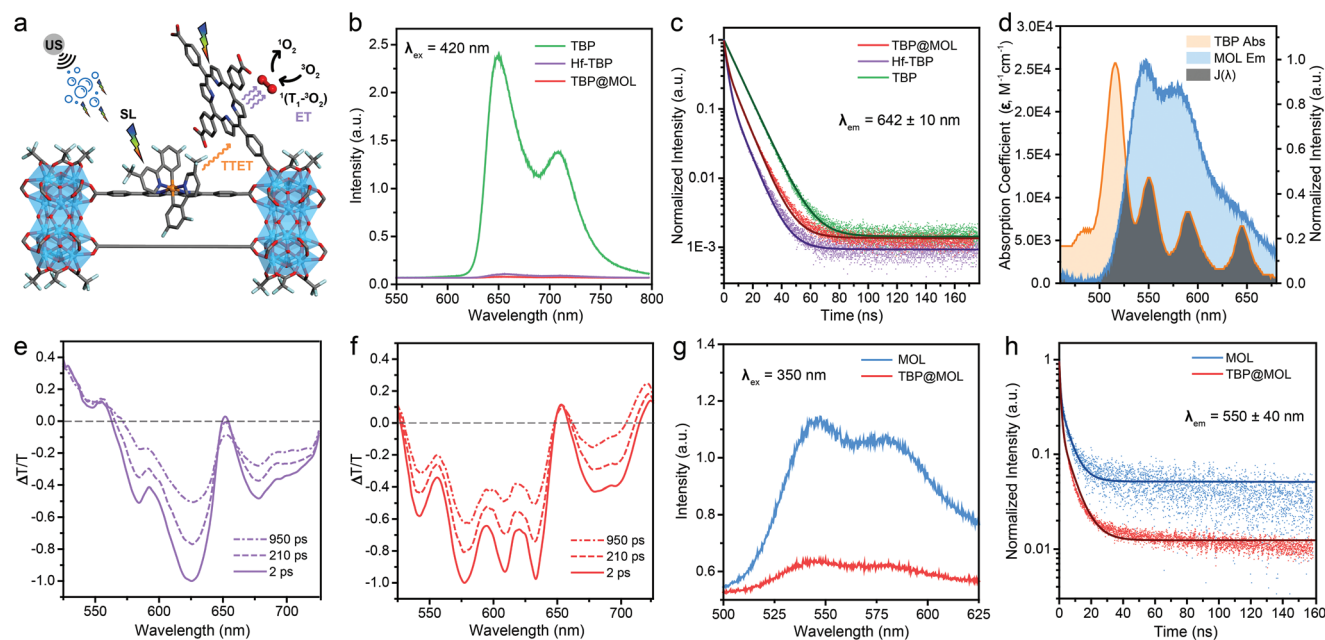
**ADVANCED
SCIENCE NEWS**

www.advancedsciencenews.com

**ADVANCED
MATERIALS**

www.advmat.de

Figure 4. a) Proposed mechanism of $^1O_2$ generation for TBP@MOL under US irradiation. DBB-Ir and TBP absorb high- and low-energy regions of the broad sonoluminescence spectrum, respectively, and the excited DBB-Ir undergoes TTET with TBP. The excited surface-anchored TBP efficiently transfers energy to $^3O_2$ for enhanced $^1O_2$ generation. b) Normalized steady-state emission and c) time-resolved emission decay spectra of the TBP systems. d) Absorption spectrum of TBP (acceptor), normalized emission spectrum of MOL (DBB-Ir; donor), and spectral overlap integral $J(\lambda)$. Transient absorption spectra of e) Hf-TBP and f) TBP@MOL at various time slices, showing the decays of the excited state absorption features. g) Normalized steady-state emission and h) time-resolved emission decay spectra of the DBB-Ir ligands in TBP@MOL and MOL.

systems under 630 nm light irradiation. Although only TBP was excited under these conditions, TBP@MOL generated 1.5-fold more $^1O_2$ than Hf-TBP (Figure 3b). We observed a negligible difference in ISC between TBP@MOL and Hf-TBP; therefore, the enhanced $^3O_2$ sensitization by TBP@MOL likely results from a higher energy transfer efficiency in the encounter complex of T_1 excited sensitizer and oxygen, $^1(T_1-{}^3O_2)$, owing to the rotational freedom and accessibility of the SBU-anchored TBP. This energy transfer proceeds via internal conversion, which plays a more decisive role than ISC,[48] eventually dissociates the $^1(T_1-{}^3O_2)$ encounter complex to afford $^1O_2$.[49–52]

We synthesized an analogous TBP-capped 2D MOL built from 1,3,5-tris(4-carboxyphenyl)benzene (BTB) linkers, TBP@Hf-BTB, to investigate the DBB-Ir contribution in SDT (Figures S25–S28, Supporting Information). Under similar US irradiation conditions, TBP@Hf-BTB generated 3.5-fold more $^1O_2$ than Hf-TBP but 2.1-fold less $^1O_2$ than TBP@MOL (Figure 3a). These results support the sonosensitization enhancement from SBU-anchored SSs as well as significant contribution from DBB-Ir linkers. Due to the proximity of TBP to DBB-Ir linkers in TBP@MOL (Figure S35, Supporting Information), we investigated the possibility of fluorescence resonance energy transfer (FRET). Spectral overlap integral [$J(\lambda)$] calculations showed that the 560 nm emission of the DBB-Ir linkers in the MOL (donor) overlaps well with the Q bands of TBP (acceptor) (Figure 4b). The steady-state emission spectra indicated quenching of the DBB-Ir emission by SBU-anchored TBP in TBP@MOL (Figure 4g). Furthermore, the TCSPC decay profile of the DBB-Ir emission in TBP@MOL displayed an additional nonradiative decay around 0.91 ns that was absent in MOL (Figure 4h; Figure S37 and Table S5, Supporting Information).

However, singlet FRET is not likely to be the major contributor to sonosensitization because, although the calculated $J(\lambda)$ of the BTB donor with the TBP acceptor in TBP@Hf-BTB doubles that of TBP@MOL (Table S7, Supporting Information), its $^1O_2$ generation is 2.1-fold lower. Since DBB-Ir has much more efficient ISC than BTB, we postulated that the enhanced $^1O_2$ generation mainly arises from triplet–triplet energy transfer (TTET) (Figures S31, S32, and S37, Supporting Information). Therefore, TBP@MOL synergistically enhances $^1O_2$ generation by direct $^3O_2$ sensitization, singlet FRET and more importantly, TTET from DBB-Ir linkers (Figure 4a).

We confirmed in vivo SDT efficacy in a CT26 colorectal adenocarcinoma mouse model and a 4T1 murine triple-negative breast cancer model (**Figure 5**a). TBP@MOL(+) exhibited outstanding SDT efficacy with tumor growth inhibition (TGI) values of 87.0% and 82.7% in CT26 and 4T1 tumor models, respectively (Figure 5b,c; Figure S53, Supporting Information). In contrast, TBP(+) displayed moderate TGI values of 25.0% and 41.5%, while Hf-TBP(+) displayed TGI values of 16.7% and 50.0% in CT26 and 4T1 models, respectively. All US-free treatment groups showed minimal efficacy (Tables S8 and S9, Supporting Information). The significantly enhanced SDT therapeutic efficacy of TBP@MOL(+) over other groups was confirmed by the smallest tumor weight among all groups at the end point (Figure 5d,e; Figures S54–S57, Supporting Information). Hematoxylin and eosin (H&E) staining and terminal deoxynucleotidyl transferase dUTP nick end labeling (TUNEL) assays showed that TBP@MOL(+) significantly reduced the density of cancerous cells and increased apoptosis in tumor slices (Figure 5f; Figures S58 and S59, Supporting Information), demonstrating enhanced
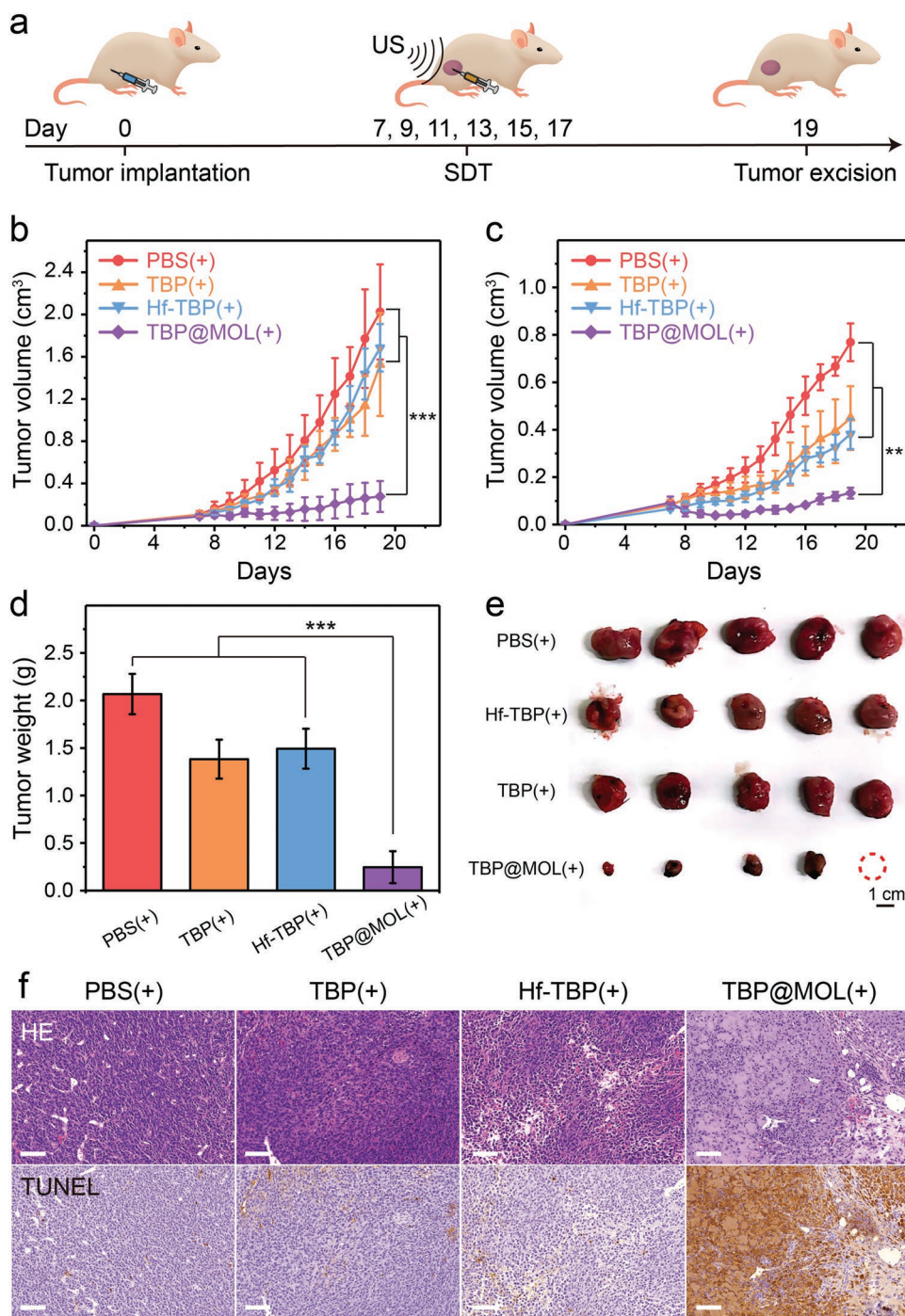
Figure 5. a) Schematic illustration of tumor inoculation and treatment schedule. SDT anticancer efficacy in subcutaneous b) CT26 and c) 4T1 tumor-bearing BALB/c mice ($n = 5$). d) Weight and e) photograph of excised CT26 tumors of BALB/c mice after PBS(+), TBP(+), Hf-TBP(+), or TBP@MOL(+) treatment. Scale bar = 1 cm. f) H&E and TUNEL staining of sectioned CT26 tumor tissues after various treatments. Scale bars = 100 μm, **, $p < 0.01$; ***, $p < 0.001$.

cancer cell killing by SDT in vivo. All treatment groups showed normal body weight trends and minimal damage in major organ sections (Figures S60–S62, Supporting Information), indicating an absence of general toxicity. Thus, TBP@MOL provides a safe and efficient platform for enhanced SDT on CT26 and 4T1 tumors.

3. Conclusion

In this work, we report a new strategy to design efficient nano-sonosensitizers based on 2D MOLs with photosensitizing iridium-based linkers and SBU-anchored TBP sonosensitizers. The TBP@MOL nano-sonosensitizer showed 14.1- and 7.4-fold

**ADVANCED
SCIENCE NEWS**

www.advancedsciencenews.com

**ADVANCED
MATERIALS**

www.advmat.de

higher $^1O_2$ generation efficacy than free TBP ligand and TBP-based MOF, respectively. As a result, TBP@MOL displayed about one order of magnitude higher cytotoxicity than free TBP ligand and TBP-based MOF under US irradiation. Spectroscopic studies indicated that TBP@MOL enhances $^1O_2$ generation by preventing aggregation-induced quenching of the excited TBP sensitizers, efficiently capturing the broad-spectrum sonoluminescence from ultrasonic cavitation via triplet–triplet Dexter energy transfer from excited DBB-Ir bridging ligands to SBU-anchored TBP SSs, and enhancing the energy transfer from the excited TBP sensitizer and $^3O_2$. TBP@MOL demonstrated significantly higher SDT efficacy than Hf-TBP and TBP in mouse models of colorectal and breast cancer.

Supporting Information

Supporting Information is available from the Wiley Online Library or from the author.

Conflict of Interest

The authors declare no conflict of interest.

Data Availability Statement

The data that support the findings of this study are available from the corresponding author upon reasonable request.

[1] A. Brotchie, *Nat. Rev. Mater.* **2017**, *2*, 17058.

[2] V. Choi, M. A. Rajora, G. Zheng, *Bioconjugate Chem.* **2020**, *31*, 967.

[3] E. Stride, C. Coussios, *Nat. Rev. Phys.* **2019**, *1*, 495.

[4] S. Son, J. H. Kim, X. Wang, C. Zhang, S. A. Yoon, J. Shin, A. Sharma, M. H. Lee, L. Cheng, J. Wu, J. S. Kim, *Chem. Soc. Rev.* **2020**, *49*, 3244.

[5] X. Qian, Y. Zheng, Y. Chen, *Adv. Mater.* **2016**, *28*, 8097.

[6] X. Lin, J. Song, X. Chen, H. Yang, *Angew. Chem., Int. Ed.* **2020**, *59*, 14212.

[7] S. Ghosh, K. A. Carter, J. F. Lovell, *Biomaterials* **2019**, *218*, 119341.

[8] L. Song, L. Lu, Y. Pu, H. Yin, K. Zhang, *Acc. Mater. Res.* **2022**, *3*, 971.

[9] S. Kwon, H. Ko, D. G. You, K. Kataoka, J. H. Park, *Acc. Chem. Res.* **2019**, *52*, 1771.

[10] S. Bai, N. Yang, X. Wang, F. Gong, Z. Dong, Y. Gong, Z. Liu, L. Cheng, *ACS Nano* **2020**, *14*, 15119.

[11] X. Lin, S. Liu, X. Zhang, R. Zhu, S. Chen, X. Chen, J. Song, H. Yang, *Angew. Chem., Int. Ed.* **2020**, *59*, 1682.

[12] L. Zhu, M. Luo, Y. Zhang, F. Fang, M. Li, F. An, D. Zhao, J. Zhang, *Coord. Chem. Rev.* **2023**, *475*, 214875.

[13] D. Li, Y. Yang, D. Li, J. Pan, C. Chu, G. Liu, *Small* **2021**, *17*, 2101976.

[14] X. Liang, M. Chen, P. Bhattarai, S. Hameed, Z. Dai, *ACS Nano* **2020**, *14*, 13569.

[15] M. Overchuk, M. Zheng, M. A. Rajora, D. M. Charron, J. Chen, G. Zheng, *ACS Nano* **2019**, *13*, 4560.

[16] X. Li, J. F. Lovell, J. Yoon, X. Chen, *Nat. Rev. Clin. Oncol.* **2020**, *17*, 657.

[17] D. Luo, K. A. Carter, E. A. G. Molins, N. L. Straubinger, J. Geng, S. Shao, W. J. Jusko, R. M. Straubinger, J. F. Lovell, *J. Controlled Release* **2019**, *297*, 39.

[18] Y. Zhang, X. Zhang, H. Yang, L. Yu, Y. Xu, A. Sharma, P. Yin, X. Li, J. S. Kim, Y. Sun, *Chem. Soc. Rev.* **2021**, *50*, 11227.

[19] A. Y. Rwei, J. L. Paris, B. Wang, W. Wang, C. D. Axon, M. Vallet-Regí, R. Langer, D. S. Kohane, *Nat. Biomed. Eng.* **2017**, *1*, 644.

[20] M. A. Rajora, J. W. H. Lou, G. Zheng, *Chem. Soc. Rev.* **2017**, *46*, 6433.

[21] P. Huang, X. Qian, Y. Chen, L. Yu, H. Lin, L. Wang, Y. Zhu, J. Shi, *J. Am. Chem. Soc.* **2017**, *139*, 1275.

[22] Z. Gong, Z. Dai, *Adv. Sci.* **2021**, *8*, 2002178.

[23] Z. Dong, Z. Feng, Y. Hao, Q. Li, M. Chen, Z. Yang, H. Zhao, Z. Liu, *Chem* **2020**, *6*, 1391.

[24] S. Liang, X. Deng, P. A. Ma, Z. Cheng, J. Lin, *Adv. Mater.* **2020**, *32*, 2003214.

[25] H. Wang, J. Guo, W. Lin, Z. Fu, X. Ji, B. Yu, M. Lu, W. Cui, L. Deng, J. W. Engle, Z. Wu, W. Cai, D. Ni, *Adv. Mater.* **2022**, *34*, 2110283.

[26] X. Zheng, L. Wang, Q. Pei, S. He, S. Liu, Z. Xie, *Chem. Mater.* **2017**, *29*, 2374.

[27] T. Luo, K. Ni, A. Culbert, G. Lan, Z. Li, X. Jiang, M. Kaufmann, W. Lin, *J. Am. Chem. Soc.* **2020**, *142*, 7334.

[28] J. Park, Q. Jiang, D. Feng, L. Mao, H.-C. Zhou, *J. Am. Chem. Soc.* **2016**, *138*, 3518.

[29] J. Park, Q. Jiang, D. Feng, H.-C. Zhou, *Angew. Chem., Int. Ed.* **2016**, *55*, 7188.

[30] X. Zheng, L. Wang, Y. Guan, Q. Pei, J. Jiang, Z. Xie, *Biomaterials* **2020**, *235*, 119792.

[31] X. Cai, Z. Xie, B. Ding, S. Shao, S. Liang, M. Pang, J. Lin, *Adv. Sci.* **2019**, *6*, 1900848.

[32] M. Lismont, L. Dreesen, S. Wuttke, *Adv. Funct. Mater.* **2017**, *27*, 1606314.

[33] P. Horcajada, R. Gref, T. Baati, P. K. Allan, G. Maurin, P. Couvreur, G. Férey, R. E. Morris, C. Serre, *Chem. Rev.* **2012**, *112*, 1232.

[34] T. Simon-Yarza, A. Mielcarek, P. Couvreur, C. Serre, *Adv. Mater.* **2018**, *30*, 1707365.

[35] Q. Xu, G. Zhan, Z. Zhang, T. Yong, X. Yang, L. Gan, *Theranostics* **2021**, *11*, 1937.

[36] Z. Xiao, Q. Chen, Y. Yang, S. Tu, B. Wang, Y. Qiu, Y. Jiang, Q. Huang, K. Ai, *Chem. Eng. J.* **2022**, *449*, 137889.

[37] F. Zhuang, Q. Ma, C. Dong, H. Xiang, Y. Shen, P. Sun, C. Li, Y. Chen, B. Lu, Y. Chen, B. Huang, *ACS Nano* **2022**, *16*, 5439.

[38] W. Wang, X. Pan, H. Yang, H. Wang, Q. Wu, L. Zheng, B. Xu, J. Wang, X. Shi, F. Bai, H. Liu, *ACS Nano* **2021**, *15*, 20003.

[39] Z.-H. Zhu, Y. Liu, C. Song, Y. Hu, G. Feng, B. Z. Tang, *ACS Nano* **2022**, *16*, 1346.

[40] G. T. Nash, T. Luo, G. Lan, K. Ni, M. Kaufmann, W. Lin, *J. Am. Chem. Soc.* **2021**, *143*, 2194.

[41] K. Lu, C. He, N. Guo, C. Chan, K. Ni, G. Lan, H. Tang, C. Pelizzari, Y.-X. Fu, M. T. Spiotto, R. R. Weichselbaum, W. Lin, *Nat. Biomed. Eng.* **2018**, *2*, 600.

[42] K. Lu, C. He, W. Lin, *J. Am. Chem. Soc.* **2014**, *136*, 16712.

[43] R. Ettlinger, U. Lächelt, R. Gref, P. Horcajada, T. Lammers, C. Serre, P. Couvreur, R. E. Morris, S. Wuttke, *Chem. Soc. Rev.* **2022**, *51*, 464.

[44] T. Luo, Y. Fan, J. Mao, E. Yuan, E. You, Z. Xu, W. Lin, *J. Am. Chem. Soc.* **2022**, *144*, 5241.

[45] C. A. Kent, B. P. Mehl, L. Ma, J. M. Papanikolas, T. J. Meyer, W. Lin, *J. Am. Chem. Soc.* **2010**, *132*, 12767.

[46] B. Marydasan, A. K. Nair, D. Ramaiah, *J. Phys. Chem. B* **2013**, *117*, 13515.

[47] R. W. Larsen, D. H. Omdal, R. Jasuja, S. L. Niu, D. M. Jameson, *J. Phys. Chem. B* **1997**, *101*, 8012.

[48] K. Kawaoka, A. U. Khan, D. R. Kearns, *J. Chem. Phys.* **1967**, *46*, 1842.

[49] D. R. Kearns, *Chem. Rev.* **1971**, *71*, 395.

[50] D. R. Kearns, A. U. Khan, *Photochem. Photobiol.* **1969**, *10*, 193.

[51] M. Bodesheim, M. Schütz, R. Schmidt, *Chem. Phys. Lett.* **1994**, *221*, 7.

[52] R. Schmidt, *Photochem. Photobiol.* **2006**, *82*, 1161.